

High-Frequency Mechanical Energy Harvester with Direct Current Output from Chemical Potential Difference

Shaoxin Li,^δ Shuo Deng,^δ Ran Xu, Di Liu, Yang Nan, Zhiwei Zhang, Yikui Gao, Haifei Lv, Min Li, Qing Zhang,* Jie Wang,* and Zhong Lin Wang*



Cite This: *ACS Energy Lett.* 2022, 7, 3080–3086



Read Online

ACCESS |



Metrics & More

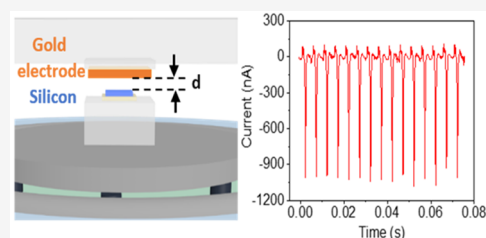


Article Recommendations



Supporting Information

ABSTRACT: As an energy harvester that converts mechanical power into electrical energy, a triboelectric nanogenerator (TENG) with a pair of metallic and insulating electrodes can generate only the displacement current (I_{dis}) in the electrodes, whereas a chemical potential difference generator (CPG) with a pair of semiconducting or/and metallic electrodes can generate both I_{dis} and conduction current (I_{con}). Considering the effects of motion parameters on I_{dis} and I_{con} is important for harvesting different mechanical energies in practical scenarios; the output characteristics of CPGs and traditional TENGs under different external resistance (R), contact-separation frequency (f), and maximum separation distance (x_m) were systematically studied for the first time in this work. More interestingly, a direct current (DC) output can be generated directly by CPGs under $R > 10 \text{ M}\Omega$ or $f > 100 \text{ Hz}$. This work not only provides a guideline for collecting different mechanical energies but also promotes the development of CPGs as an energy harvester and self-powered vibration sensor in the semiconductor industry.



With the rapid development of the electronic intelligence age, self-powered energy devices are desired and needed for a large number of miniaturized, portable, and wireless electronic devices.^{1–3} For continuous operation of these devices, it is important to develop microelectric generators that can convert mechanical energy into electricity.^{4–7} Triboelectric nanogenerators (TENGs) are a type of promising mechanical-to-electric power converters with the advantages of low-cost, wide choice of materials, and simple fabrication.^{8–12} A typical TENG is composed of a pair of insulating and insulating or metallic electrodes.^{13,14} The two electrodes are charged with equal opposite charges when they contact with each other because of triboelectrification.^{15–17} Then, electrons transfer back and forth between the backside metallic pad of the two electrodes through the external circuit because of electrostatic induction, realizing the conversion from mechanical power to electrical energy.^{18–20} However, only displacement current (I_{dis}) is generated between the two electrodes; the insulating electrode simply blocks electrons from passing across the surfaces of the two electrodes. I_{dis} is capacitively coupled to the external circuits so that the power delivered to the external resistance is determined by the internal impedance of the TENG, actual variation of the capacitance (C) between the two electrodes, parasitic capacitance, and external resistance. Although a large C is desirable to accommodate more charges, a large time

constant RC reduces the power conversion efficiency,^{21,22} where R is the external load resistance. The I_{dis} of TENG is also suppressed by a large R because of the slow charging process.²² More importantly, this problem would become more critical under high f and small x_m , in which x_m is the maximum gap between two electrodes, causing the degradation of the output performance of the TENG.

In 2018, a unique electric generator with a pair of semiconducting and semiconducting or metallic electrode dynamics was reported.²³ The two electrodes must have a distinct chemical potential difference. When the two electrodes are brought in contact, electrons diffuse from the higher to the lower chemical potential electrode.^{24,25} Once both electrodes are separated by mechanical power, the diffused electrons can be pumped out to the external circuit, yielding a transient current through the external load. In the approaching stage, apart from that through electrostatic induction (causing I_{dis}), the space charge regions near the surfaces of the electrodes can

Received: July 12, 2022

Accepted: August 23, 2022

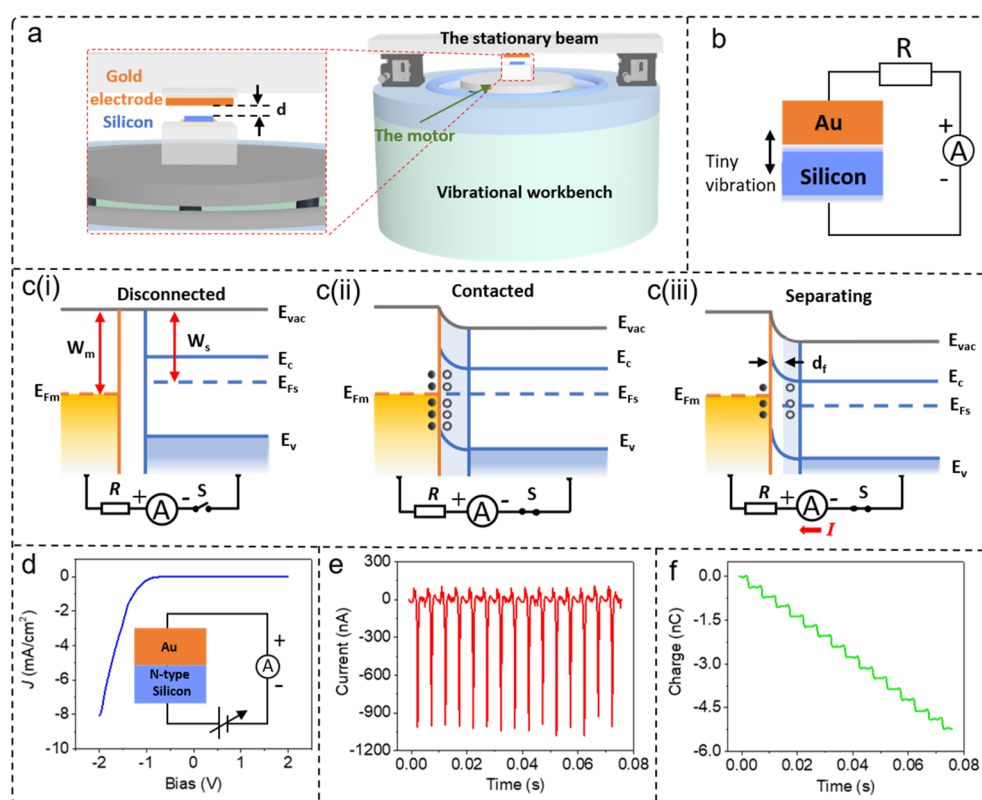


Figure 1. The experimental setup and output performance of a CPG with an electrode pair of Au and n-type Si electrodes. (a) Structure of experimental setup. The components of the CPG are shown in the enlarged illustration on the left. (b) Circuit connection in this experiment. (c) Detailed energy band diagram of CPG in (i) disconnected, (ii) contacted, and (iii) separating state. (d) The static J - V curve between the contacted Au and n-type Si electrode pair. Inset: the circuit for the J - V curve measurement. (e and f) The current output characteristic and the accumulative charge of the CPG under $R = 5 \text{ M}\Omega$, $f = 200 \text{ Hz}$, and $x_m = 0.3 \text{ mm}$.

also be restored through diffusion of electrons across the contacted surfaces, leading to a conduction current (I_{con}). As R increases, the charge collected through I_{con} of the chemical potential difference generator (CPG) does not vary significantly while the charge collected from I_{dis} is gradually decreased, even dropping to an undetectable level under $R \approx 100 \text{ M}\Omega$.² The CPG does demonstrate several unique characteristics for mechanical power-to-electricity conversion. However, critical parameters affecting the electrical performance of CPG, including R , x_m , and f , have not been systematically investigated to the best of our knowledge.

Here, the influences of R , x_m , and f on the performances of both typical CPG and TENG under a vertical contact separation motion mode are compared systematically. It is found that the increasing of R and f causes the alternating current (AC) output of the TENG to decrease gradually, while inducing a direct current (DC) output for the CPG. This contrasting characteristic demonstrates that the RC effect inhibits I_{dis} but has much less impact on I_{con} . Beyond high f , the hundred micrometer x_m is a remarkable merit of the CPG for obtaining high-frequency and tiny mechanical vibration energy. The proposed systematic comparison of TENG and CPG not only provide a guideline for harvesting different mechanical energy but also demonstrates the potential prospects of CPG as a new energy harvester or self-powered vibration sensor in the era of semiconductor integrated electronic intelligence.

In order to investigate the output electrical characteristic of CPG under different R , f and x_m , we set up a contact-

separation experimental platform as shown in Figure 1a. An n-type silicon (Si) electrode, whose doping concentration (N_d) and thickness are 5×10^{15} to $6 \times 10^{14} \text{ cm}^{-3}$ and $541 \mu\text{m}$ (Figure S1), is fixed on the center of the mover of a vibrational workbench. A gold (Au) electrode is fixed on the stationary beam. The size of the contact area between the two electrodes is about $5 \text{ mm} \times 5 \text{ mm}$. Two miniature lifting displacement platforms with two screw micrometers (Figure 1a) are used to maintain a proper tiny gap between the two electrodes. Figure 1b shows the circuit connect between two electrodes of CPG and the ammeter SRS70 in this experiment. The energy band diagrams of the n-type Si electrode and Au electrode under disconnected and contacted stages are sketched in Figure 1c(i,ii). A positive space charge or depletion layer formed near the contacted n-type Si electrode surface because of their chemical potential difference. Once the two electrodes are separated from each other (Figure 1c(iii)), the depletion region narrows significantly and the Fermi level of the Si electrode (E_{Fs}) drops below the Fermi level of Au electrode (E_{Fm}), as the positive charges trapped in charge space are pumped to the external circuit. Therefore, a negative transient current flows from the n-type Si electrode to the Au electrode through R , realizing the conversion of mechanical power to electrical energy. A very good rectification characteristic of the J - V curve is obtained when the two electrodes are in static contact (Figure 1d), suggesting that a decent Schottky junction is formed. Figure 1e displays the output current of CPG under $R = 5 \text{ M}\Omega$, $f = 200 \text{ Hz}$, and $x_m = 0.3 \text{ mm}$. The current output of about 900 nA is generated directly by the CPG, and it is

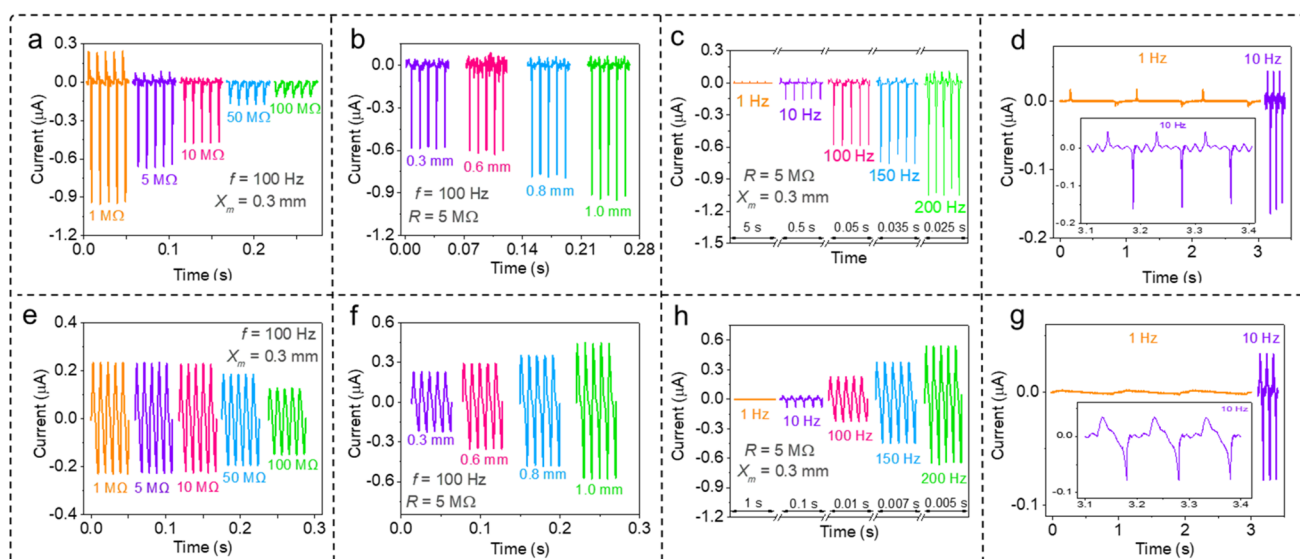


Figure 2. Output current characteristics of a CPG and a TENG under different movement conditions. (a and e) The output current of the CPG and TENG vs R under $f = 100$ Hz and $x_m = 0.3$ mm. (b and f) The output current of the CPG and TENG vs x_m under $f = 100$ Hz and $R = 5$ M Ω . (c and g) The output current of the CPG and TENG vs f under $R = 5$ M Ω and $x_m = 0.3$ mm. (d and h) Detailed output current of the CPG and TENG under $f = 1$ Hz and $f = 10$ Hz in 3 periods.

apparently a pulsed DC current. The accumulative charge collected from the current (Figure 1f) indicates that the transferred charge during one cycle is up to about 0.4 nC.

Figure 2a–c exhibits the measured output current versus R , f , and x_m for the CPG, respectively. Under $f = 100$ Hz and $x_m = 0.3$ mm (Figure 2a), the positive current almost reduces to about 0 μ A under $R = 5$ M Ω , while the intensity of negative current just decreased 0.3 μ A compared to $R = 1$ M Ω . Although the intensity of negative current decreases with increasing R , the CPG keeps the DC output for R higher than 5 M Ω . The output current of CPG with different x_m under $R = 5$ M Ω and $f = 100$ Hz is shown in Figure 2b. The peak current output increases from 0.6 to 0.9 μ A with the x_m changing from 0.3 to 1.0 mm. Meanwhile, the output current of CPG with different f under $R = 5$ M Ω and $x_m = 0.3$ mm is shown in Figure 2c. With f increasing from 1 to 100 Hz, the peak output current increase from 0.01 μ A to 0.6 μ A. Then, the output current intensity remains unchanged with f increasing from 100 Hz to 200 Hz. More importantly, it is observed that the output current is dominated by a pulsed DC current for f higher than 100 Hz. To compare the output performance of the CPG with that of a traditional TENG, the TENG mainly consists of a Au electrode and a poly tetra fluoroethylene (PTFE) film coated with a Au film on the back for the electric connection with the external circuit. The contact area of the two electrodes and the thickness of PTFE film in the TENG is about 5 mm \times 5 mm and 541 μ m, comparable to those used in the CPG (Figure S1). With R , f , and x_m increasing, the output current of TENG keeps an AC style (Figure 2e–h). Moreover, the equal amount of electrons transferred between the two electrodes during the contact and separation processes also demonstrates the AC characteristics of the TENG under different movement variables (Figure S2). The output current decreases with R increasing, while it increases with increasing x_m and f . As shown in Figure 2d,g, it is noted that the pulse width of the current shrinks significantly as f increases.

The working mechanisms and output current characteristics of the CPG and TENG under $R = 5$ M Ω , $f = 200$ Hz, and $x_m = 0.3$ mm are illustrated in Figure 3. For the CPG, when

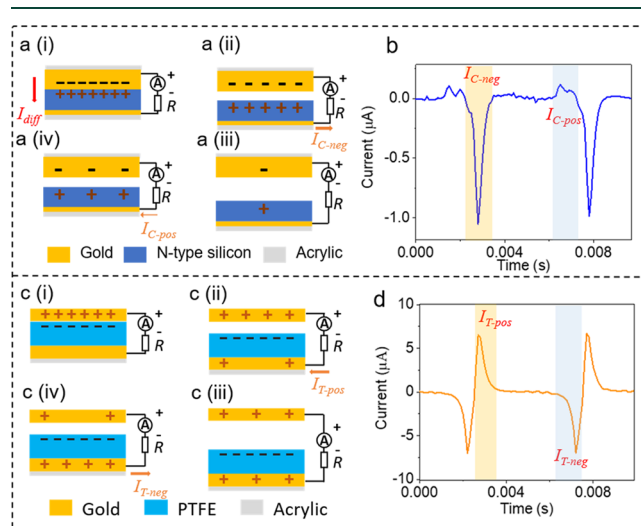


Figure 3. Working mechanisms of the CPG and TENG under $R = 5$ M Ω , $f = 200$ Hz, and $x_m = 300$ μ m. (a) Schematic illustration of the current generation in a contact and separation cycle for the CPG. (b) Output current of the CPG as a function of time. (c) Schematic illustration of the current generation in a contact and separation cycle for the TENG. (d) Output current of the TENG as a function of time.

the two electrodes are brought in contact, electrons in the n-type Si electrode transfer to the Au electrode because of their chemical potential difference (Figure 3a(i)). Once the Au electrode leaves from the Si electrode under mechanical power, the electrons discharge from the Au electrode to the n-type Si electrode through the external circuit to balance the electrical potential difference between the two electrodes (Figure 3a(ii)). Until the separation distance is larger than the width of the depletion region of the n-type Si electrode, most of the

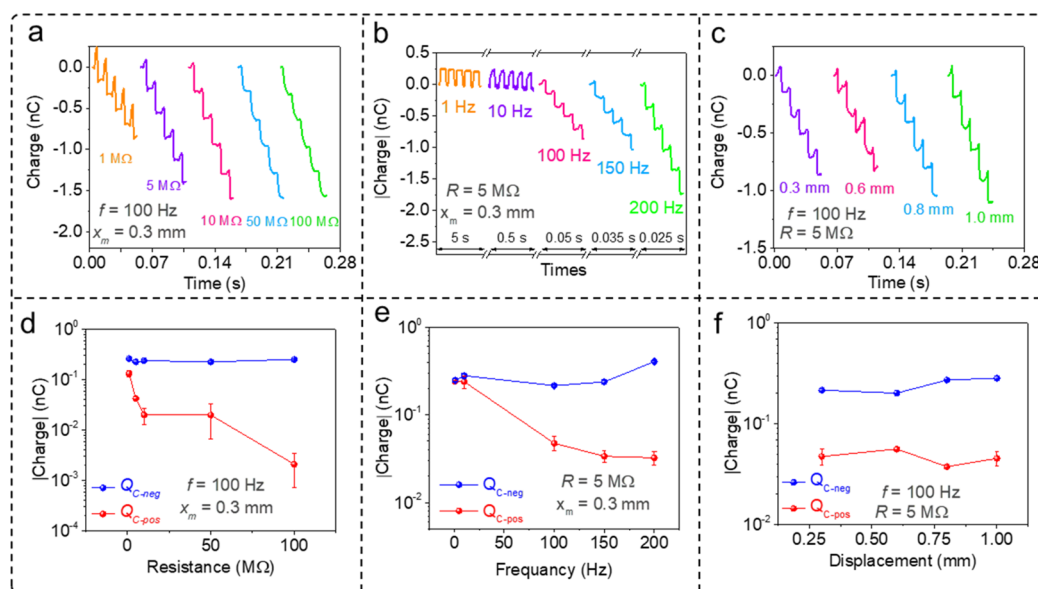


Figure 4. Accumulated charge of the CPG under different conditions. (a) The original charge signals vs R under $f = 100$ Hz and $x_m = 0.3$ mm. (b) Original charge signals vs f under $R = 5$ M Ω and $x_m = 0.3$ mm. (c) The original charge signals vs x_m under $R = 5$ M Ω and $f = 100$ Hz. (d) The $Q_{C\text{-neg}}$ and $Q_{C\text{-pos}}$ vs R under $f = 100$ Hz and $x_m = 0.3$ mm. (e) The $Q_{C\text{-neg}}$ and $Q_{C\text{-pos}}$ vs f under $R = 5$ M Ω and $x_m = 0.3$ mm. (f) The $Q_{C\text{-neg}}$ and $Q_{C\text{-pos}}$ vs x_m under $R = 5$ M Ω and $f = 100$ Hz.

electrons in the depletion region have been pumped out to the external circuit.²³ A temporary thermal equilibrium state could establish when the gap reaches the maximum (Figure 3a(iii)). In the approaching stage (Figure 3a(iv)), the space charge region in the n-type Si electrode could restore through the chemical potential difference of the two electrodes, causing a positive I_{dis} flowing from the Au electrode to the n-type Si electrode. This current increases until the two electrodes are just in contact. Thereafter, the space charge region can also restore through diffusion of electrons from the n-type Si electrode to the Au electrode, yielding I_{con} , which is not measurable in the external circuit. For our Au and n-type Si electrode pairs, the $RC = 3.0 \times 10^{-3}$ s under the $R = 5$ M Ω and the $C = 6.15 \times 10^{-10}$ F (the detailed measurement method is shown in Experimental Methods in the Supporting Information). Under $f = 200$ Hz, the time of approaching stage $t_{\text{app}} = 2.5 \times 10^{-3}$ s is comparable with that of RC . As a result, the space charge region cannot fully restore in the approaching stage and then the rest space charge region restoration would proceed with electron diffusion after the two electrodes are in contact. It is the existence of the diffusion current across the two contacted electrode surfaces that leads to generation of the DC-dominated pulsed current by the CPG (Figure 3b). In sharp contrast, for the TENG, when the two electrodes fully contact with each other, electrons transfer from the Au electrode to the PTFE surface because of the electron affinity difference between the two electrodes, resulting in a negatively charged PTFE surface and positively charged Au electrode (Figure 3c(i)).^{26–28} Once the Au electrode separates from the PTFE electrode under mechanical power, the positive charge on the Au electrode is gradually neutralized by electrons from the back Au film of the PTFE electrode, resulting in a gradual increase in positive charge in the back Au film, to balance their potential difference (Figure 3c(ii)). Figure 3c(iii) shows the charge distribution between the two electrodes, when the separation reaches its maximum of 0.3 mm. Next,

electrons flow back to the Au electrode from the back Au film in the approaching stage to decrease the potential difference between the two electrodes until both electrodes get in contact (Figure 3c(iv)). Therefore, electrons transfer back and forth between the Au electrode and back Au film to form an AC current in the external circuit (Figure 3d).^{29,30} It is worth noting that the AC output of TENG is displacement current, $\frac{\partial P}{\partial t}$, arising from the polarization field generated by the electrostatic charge on the surface, which is termed the Wang term.³¹ According to the theoretical mode of TENG (Figure S3), the electrical filed inside the dielectric PTFE (E_1) can be described as follows:²¹

$$E_1 = -\frac{Q(t)}{S\epsilon_0\epsilon_{r1}} \quad (1)$$

where $Q(t)$ is the charge of the back Au film, S the contact area of the Au electrode, ϵ_0 the vacuum dielectric constant, and ϵ_{r1} the relative dielectric constant of the PTFE. The electric field inside the air gap E_{air} is

$$E_{\text{air}} = \frac{-\frac{Q(t)}{S} + \sigma}{\epsilon_0} \quad (2)$$

where σ is the electrostatic charge density on the surface of the PTFE and can be treated as a constant after several contact–separation cycles. The voltage drop for R is $V = IR = R\frac{dQ}{dt}$ or

$$R\frac{dQ}{dt} = -\frac{Q}{S\epsilon_0}(d_0/\epsilon_r + x(t)) + \frac{\sigma x(t)}{\epsilon_0} \quad (3)$$

The detailed parameters used in the simulation are listed in Tables S1–S3. The calculated results indicate that R has an inhibitory effect on the output current intensity of TENG (Figure S4), while high f and large x_m can increase the output current intensity of TENG, which is consistent with the experimental results as shown in Figure 2d–f.

The influences of R , f , and x_m on the accumulative charge for the CPG are shown in Figure 4. As the CPG under large R ($>5\text{ M}\Omega$) or high f ($>100\text{ Hz}$), the charge versus time curve shows a step-like shape (Figure 4a,b). When $R = 5\text{ M}\Omega$, $f = 100\text{ Hz}$, and $x_m = 0.3\text{ mm}$, the average charge per cycle is about 0.3 nC . The output charge increases with the extension of x_m (Figure 4c), accompanied by the increase of output current as shown in Figure 2c. The charges collected during the negative current ($Q_{C\text{-neg}}$) and positive current ($Q_{C\text{-pos}}$)

through $Q_{C\text{-neg(C-pos)}} = \int_0^{t_{\text{app}}} I_{C\text{-neg(C-pos)}} dt$ are shown in Figure 4d. It is seen that $Q_{C\text{-pos}}$ sharply decreases from about 0.1 nC under $R = 1\text{ M}\Omega$ to 0.002 nC under $R = 100\text{ M}\Omega$, while $Q_{C\text{-neg}}$ remains about 0.1 nC , nearly independent of R . This result clearly suggests that under a large R , the depletion region of the Schottky junction is restored through electron diffusion across the contacted surfaces, thus a large R has no inhibiting effect on I_{con} . Here, the ratio of $Q_{C\text{-neg}}/Q_{C\text{-pos}}$ increases from 2 to 1.2×10^2 for R from $1\text{ M}\Omega$ up to $100\text{ M}\Omega$, demonstrating a DC output performance of the CPG under a larger R . Additionally, from Figure 4e one can see that the higher f also hinders $Q_{C\text{-pos}}$ but has no effect on $Q_{C\text{-neg}}$. The $Q_{C\text{-pos}}$ gradually decreases from about 0.2 nC under $f = 1\text{ Hz}$ to 0.03 nC under $f = 200\text{ Hz}$ simply because restoration of the depletion region becomes more difficult via electrostatic induction under a higher f in the approaching stage. When x_m increases from 0.3 mm to 1.0 mm under $f = 100\text{ Hz}$ and $R = 5\text{ M}\Omega$, $Q_{C\text{-neg}}$ maintains around 0.2 nC (Figure 4f). As x_m is much larger than the depletion layer width (W_D) of the Schottky junction,³² it is reasonable that $Q_{C\text{-neg}}$ and $Q_{C\text{-neg}}/Q_{C\text{-pos}}$ do not apparently change with x_m , as shown in Figure 4f.

Furthermore, the influence of the work function for different metal electrodes (copper (Cu), Au, platinum (Pt)) on the current output of CPGs have been studied (Figure 5). The well-accepted work functions of Cu, Au, Pt are 4.3, 4.8, and 5.3 eV, respectively.³³ Using the variable capacitance method,²³ the chemical potential difference (V_B) between the n-type Si and the metal electrodes are measured to be 0.08 V for the Cu and n-type Si, 0.46 V for the Au and n-type Si, and 0.57 V for the Pt and n-type Si electrode pair (Figure S5). Figure 5a shows the static J - V curve of each of the electrode pairs. Their good rectification characteristics suggest that the Schottky junctions can well form in the three static contacted electrode pairs. The rectification factor, i.e., $|I(+4.0\text{V})/I(-4.0\text{V})|$ for the Cu and n-type Si electrode pair is about 2.6, lower than the 5.5 for the Pt and n-type Si and 4.8 for Au and n-type Si electrode pair. The output current and $Q_{C\text{-neg}}$ of each of the electrode pairs under $R = 5\text{ M}\Omega$, $f = 200\text{ Hz}$, and $x_m = 0.3\text{ mm}$ are shown in panels b and c of Figure 5, respectively. A pulse DC dominated output can be observed from these electrode pairs. The current peak intensity of the Cu and n-type Si electrode pair is about 360 nA , which is obviously lower than that of the Pt and n-type Si and Au and n-type Si electrode pairs (560 nA). The value of $Q_{C\text{-neg}}$ follows the trend of Pt and n-type Si $>$ Au and n-type Si $>$ Cu and n-type Si, suggesting that a larger V_B may promote a higher

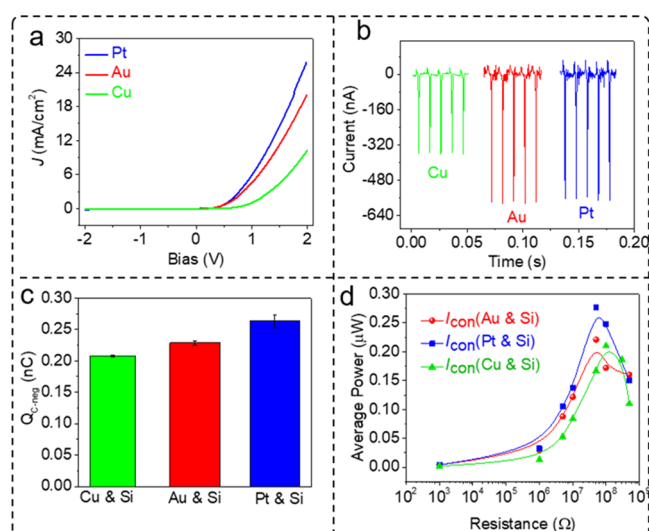


Figure 5. The output performance of CPGs for the Pt and n-type Si, Au and n-type Si, and Cu and n-type Si electrode pairs. (a) The J - V curves. (b) The output currents under $R = 5\text{ M}\Omega$, $f = 200\text{ Hz}$, and $x_m = 0.3\text{ mm}$. (c) The accumulative charges for a single negative pulse current ($Q_{C\text{-neg}}$). (d) The average power for the DC output as a function of R .

electron pumping capability. This result is consistent with the prior result that $Q_{C\text{-neg}}$ is proportional to the V_B :²³

$$Q_{C\text{-neg}} \approx \frac{2V_B \epsilon_0 \epsilon_r S}{W_n} \quad (4)$$

where W_n is the depletion region width in the n-type Si electrode. The negative current average power $\bar{P} = R \int_0^{t_s} i^2 dt / t_s$ versus R for these metal electrodes under $f = 200\text{ Hz}$ is shown in Figure 5d, where t_s is the time duration of the pulse current. The \bar{P} of Cu and n-type Si, Au and n-type Si, and Pt and n-type Si are $0.21\text{ }\mu\text{W}$ at $R = 100\text{ M}\Omega$, $0.22\text{ }\mu\text{W}$ at $R = 50\text{ M}\Omega$, and $0.27\text{ }\mu\text{W}$ at $R = 50\text{ M}\Omega$, respectively.

Taking the Au and n-type Si electrode pair as an ideal Schottky contact, the charge stored in the depletion region $Q_S \approx qN_D A \sqrt{2\epsilon_0 \epsilon_r V_B / (qN_D)} \sim 1 \times 10^{-6}\text{ C}$, which is about 4 orders of magnitude higher than the $Q_{C\text{-neg}}$ per cycle observed in Figure 4. Under the nonideal Schottky contact, the surface states induce a potential barrier in the contact interface, which inhibits the carrier transfer between the Au and n-type Si electrode.³² This is the reason why the output improvement of the Au and n-type Si electrode pair is not significant compared with that of the Cu and n-type Si electrode pair, although the chemical potential difference of Au and n-type Si electrode (0.46 eV) is much higher than that of Cu and n-type Si electrode pair (0.08 eV). Moreover, a small air gap of several nanometers in the contacted state could result in a sharp decrease of charge stored in the depletion region.³²

In this work, the effects of R , x_m , and f on the current output of CPGs and TENGs have been first systematically studied. As a result, the TENG is shown to be suitable for harvesting ambient energy with low f and large x_m , such as ocean energy, human motion energy, etc., whereas the CPG is capable of harvesting mechanical energy with high f and tiny x_m , such as sonic energy. Different from the TENG, the output current of CPGs is dominated by discharging the diffused

electrons to the load, rather than from discharging electrostatically induced charges, leading to the output performance of the CPG being independent with the time constant RC , which is one of the merits of CPGs. Therefore, a pulse DC output can be directly generated by a CPG under a large R ($> 10M\Omega$) or high f (>100 Hz), which demonstrates the potential application of the CPG as a high-frequency energy harvester in the semiconductor industry. Taking advantage of its signal characteristics from low to high frequency, the CPG is also expected to be a self-powered vibration and threshold monitoring sensor with a wide frequency response range. CPGs also have the potential to be used as an energy harvester or sensor for micromagnitude and high-frequency vibrations. In conclusion, this work not only provides clear guidance for obtaining different mechanical energies through TENGs or CPGs but also provides a practical paradigm for further establishing the physical model of CPGs.

■ ASSOCIATED CONTENT

SI Supporting Information

The Supporting Information is available free of charge at <https://pubs.acs.org/doi/10.1021/acsenerylett.2c01582>.

Additional experimental descriptions of electrode preparation of CPG, fabrication of TENG, construction of vibration test bench, electrical characteristic measurement, capacitance measurement of the electrode pairs, and calculation process of Simulink of TENG capacitance model; SEM cross section of silicon and PTFE; theoretical mode of the TENG; calculated output current characteristics of the TENG; determination of the chemical potential difference V_B between the metal and n-type Si electrode; calculation parameters of TENG versus different R ; calculation parameters of TENG vs different f ; calculation parameters of TENG versus different x_m (PDF)

■ AUTHOR INFORMATION

Corresponding Authors

Qing Zhang – School of Electrical & Electronic Engineering, Nanyang Technological University, Singapore 639798, Singapore; Email: eqzhang@ntu.edu.sg

Jie Wang – Beijing Institute of Nanoenergy and Nanosystems, Chinese Academy of Sciences, Beijing 100083, P. R. China; School of Nanoscience and Technology, University of Chinese Academy of Sciences, Beijing 100049, P. R. China; orcid.org/0000-0003-4470-6171; Email: wangjie@binn.cas.cn

Zhong Lin Wang – Beijing Institute of Nanoenergy and Nanosystems, Chinese Academy of Sciences, Beijing 100083, P. R. China; School of Nanoscience and Technology, University of Chinese Academy of Sciences, Beijing 100049, P. R. China; School of Materials Science and Engineering, Georgia Institute of Technology, Atlanta, Georgia 30332, United States; orcid.org/0000-0002-5530-0380; Email: zhong.wang@mse.gatech.edu

Authors

Shaixin Li – Beijing Institute of Nanoenergy and Nanosystems, Chinese Academy of Sciences, Beijing 100083, P. R. China; School of Nanoscience and Technology, University of Chinese Academy of Sciences, Beijing 100049, P. R. China

Shuo Deng – Department of Physics, Wuhan University of Technology, Wuhan 430070, P. R. China

Ran Xu – School of Electrical & Electronic Engineering, Nanyang Technological University, Singapore 639798, Singapore

Di Liu – Beijing Institute of Nanoenergy and Nanosystems, Chinese Academy of Sciences, Beijing 100083, P. R. China; School of Nanoscience and Technology, University of Chinese Academy of Sciences, Beijing 100049, P. R. China

Yang Nan – Beijing Institute of Nanoenergy and Nanosystems, Chinese Academy of Sciences, Beijing 100083, P. R. China; School of Nanoscience and Technology, University of Chinese Academy of Sciences, Beijing 100049, P. R. China; orcid.org/0000-0002-2504-2982

Zhiwei Zhang – Beijing Institute of Nanoenergy and Nanosystems, Chinese Academy of Sciences, Beijing 100083, P. R. China; School of Nanoscience and Technology, University of Chinese Academy of Sciences, Beijing 100049, P. R. China

Yikui Gao – Beijing Institute of Nanoenergy and Nanosystems, Chinese Academy of Sciences, Beijing 100083, P. R. China

Haifei Lv – Department of Physics, Wuhan University of Technology, Wuhan 430070, P. R. China

Min Li – Department of Physics, Wuhan University of Technology, Wuhan 430070, P. R. China

Complete contact information is available at:

<https://pubs.acs.org/10.1021/acsenerylett.2c01582>

Author Contributions

[§]S.L. and S.D. contributed equally to this work.

Notes

The authors declare no competing financial interest.

■ ACKNOWLEDGMENTS

This project is financially supported by National Key Research and Development Program of China for Young Scientists (2021YFF0603500), National Natural Science Foundation of China (11974266 and U21A20147), Fundamental Research Funds for the Central Universities (WUT:2022IVA061, E1E46802), A*STAR AME IRG Grant SERC A1983c0027, and MOE AcRF Tier2 (2018-T2-2-005), Singapore.

■ REFERENCES

- (1) Tang, X.; Wang, X.; Cattley, R.; Gu, F.; Ball, A. D. Energy harvesting technologies for achieving self-powered wireless sensor networks in machine condition monitoring: A review. *Sensors* **2018**, *18*, 4113.
- (2) Elahi, H.; Munir, K.; Eugeni, M.; Atek, S.; Gaudenzi, P. Energy harvesting towards self-powered IoT devices. *Energies* **2020**, *13*, 5528.
- (3) Niu, S.; Wang, X.; Yi, F.; Zhou, Y. S.; Wang, Z. L. A universal self-charging system driven by random biomechanical energy for sustainable operation of mobile electronics. *Nat. Commun.* **2015**, *6*, 8975.
- (4) Xue, X.; Wang, S.; Guo, W.; Zhang, Y.; Wang, Z. L. Hybridizing energy conversion and storage in a mechanical-to-electrochemical process for self-charging power cell. *Nano Lett* **2012**, *12*, 5048–5054.
- (5) Zhang, Q. Roles of Semiconductor Junctions in Mechanical-Electrical Power Conversion. In *Proceedings of the 4th IEEE Electron Devices Technology & Manufacturing Conference*; EDTM, 2020; pp 1–4.
- (6) Xu, R.; Zhang, Q.; Wang, J. Y.; Liu, D.; Wang, J.; Wang, Z. L. Direct current triboelectric cell by sliding an n-type semiconductor on a p-type semiconductor. *Nano Energy* **2019**, *66*, 104185.

- (7) Yang, R.; Xu, R.; Dou, W.; Benner, M.; Zhang, Q.; Liu, J. Semiconductor-based dynamic heterojunctions as an emerging strategy for high direct-current mechanical energy harvesting. *Nano Energy* **2021**, *83*, 105849.
- (8) Chen, J.; Wang, Z. L. Reviving vibration energy harvesting and self-powered sensing by a triboelectric nanogenerator. *Joule* **2017**, *1*, 480–521.
- (9) Wu, C.; Wang, A. C.; Ding, W.; Guo, H.; Wang, Z. L. Triboelectric nanogenerator: a foundation of the energy for the new era. *Adv. Energy Mater.* **2019**, *9*, 1802906.
- (10) Wang, Z. L. Triboelectric nanogenerator (TENG)—sparking an energy and sensor revolution. *Adv. Energy Mater.* **2020**, *10*, 2000137.
- (11) Liu, D.; Yin, X.; Guo, H.; Zhou, L.; Li, X.; Zhang, C.; Wang, J.; Wang, Z. L. A constant current triboelectric nanogenerator arising from electrostatic breakdown. *Sci. Adv.* **2019**, *5*, No. eaav6437.
- (12) Wang, Z. L. Triboelectric nanogenerators as new energy technology and self-powered sensors—Principles, problems and perspectives. *Faraday Discuss.* **2014**, *176*, 447–458.
- (13) Zi, Y.; Wang, J.; Wang, S.; Li, S.; Wen, Z.; Guo, H.; Wang, Z. L. Effective energy storage from a triboelectric nanogenerator. *Nat. Commun.* **2016**, *7*, 10987.
- (14) Cui, N.; Gu, L.; Lei, Y.; Liu, J.; Qin, Y.; Ma, X.; Hao, Y.; Wang, Z. L. Dynamic behavior of the triboelectric charges and structural optimization of the friction layer for a triboelectric nanogenerator. *ACS Nano* **2016**, *10*, 6131–6138.
- (15) Luo, N.; Feng, Y.; Zhang, L.; Sun, W.; Wang, D.; Sun, X.; Zhou, F.; Liu, W. Controlling the tribological behavior at the friction interface by regulating the triboelectrification. *Nano Energy* **2021**, *87*, 106183.
- (16) Zhou, L.; Liu, D.; Li, S.; Zhao, Z.; Zhang, C.; Yin, X.; Liu, L.; Cui, S.; Wang, Z. L.; Wang, J. Rationally designed dual-mode triboelectric nanogenerator for harvesting mechanical energy by both electrostatic induction and dielectric breakdown effects. *Adv. Energy Mater.* **2020**, *10*, 2000965.
- (17) Wang, Z. L.; Wang, A. C. On the origin of contact-electrification. *Mater. Today* **2019**, *30*, 34–51.
- (18) Kim, W.-G.; Kim, D.-W.; Tcho, I.-W.; Kim, J.-K.; Kim, M.-S.; Choi, Y.-K. Triboelectric nanogenerator: structure, mechanism, and applications. *ACS Nano* **2021**, *15*, 258–287.
- (19) Zhou, L.; Liu, D.; Wang, J.; Wang, Z. L. Triboelectric nanogenerators: fundamental physics and potential applications. *Friction* **2020**, *8*, 481–506.
- (20) Wang, Z. L. On Maxwell's displacement current for energy and sensors: the origin of nanogenerators. *Mater. Today* **2017**, *20*, 74–82.
- (21) Niu, S.; Wang, S.; Lin, L.; Liu, Y.; Zhou, Y. S.; Hu, Y.; Wang, Z. L. Theoretical study of contact-mode triboelectric nanogenerators as an effective power source. *Energy Environ. Sci.* **2013**, *6*, 3576–3583.
- (22) Niu, S.; Wang, Z. L. Theoretical systems of triboelectric nanogenerators. *Nano Energy* **2015**, *14*, 161–192.
- (23) Zhang, Q.; Xu, R.; Cai, W. Pumping electrons from chemical potential difference. *Nano Energy* **2018**, *51*, 698–703.
- (24) Kuehne, I.; Frey, A.; Marinkovic, D.; Eckstein, G.; Seidel, H. Power MEMS—a capacitive vibration-to-electrical energy converter with built-in voltage. *Sens. Actuators A Phys.* **2008**, *142*, 263–269.
- (25) Varpula, A.; Laakso, S. J.; Havia, T.; Kynnäräinen, J.; Prunnila, M. Harvesting vibrational energy using material work functions. *Sci. Rep.* **2015**, *4*, 6799.
- (26) Xu, C.; Zi, Y.; Wang, A. C.; Zou, H.; Dai, Y.; He, X.; Wang, P.; Wang, Y. C.; Feng, P.; Li, D.; et al. On the electron-transfer mechanism in the contact-electrification effect. *Adv. Mater.* **2018**, *30*, 1706790.
- (27) Zhang, C.; Tang, W.; Zhang, L.; Han, C.; Wang, Z. L. Contact electrification field-effect transistor. *ACS Nano* **2014**, *8*, 8702–8709.
- (28) Wang, Z. L. From contact-electrification to triboelectric nanogenerators. *Rep. Prog. Phys.* **2021**, *84*, 096502.
- (29) Yang, B.; Zeng, W.; Peng, Z. H.; Liu, S. R.; Chen, K.; Tao, X. M. A fully verified theoretical analysis of contact-mode triboelectric nanogenerators as a wearable power source. *Adv. Energy Mater.* **2016**, *6*, 1600505.
- (30) Chen, H.; Xu, Y.; Zhang, J.; Wu, W.; Song, G. Theoretical system of contact-mode triboelectric nanogenerators for high energy conversion efficiency. *Nanoscale Res. Lett.* **2018**, *13*, 346.
- (31) Wang, Z. L. On the expanded Maxwell's equations for moving charged media system—General theory, mathematical solutions and applications in TENG. *Mater. Today* **2022**, *52*, 348–363.
- (32) Deng, S.; Xu, R.; Li, M.; Li, L.; Wang, Z. L.; Zhang, Q. Influences of surface charges and gap width between p-type and n-type semiconductors on charge pumping. *Nano Energy* **2020**, *78*, 105287.
- (33) Sze, S. M.; Ng, K. K. In *Physics of Semiconductor Devices*; John Wiley & Sons, 2007.